Physics in Medicine & Biology

NOTE • OPEN ACCESS

High resolution propagation-based imaging system for *in vivo* dynamic computed tomography of lungs in small animals

To cite this article: M Preissner *et al* 2018 *Phys. Med. Biol.* **63** 08NT03

IOP Publishing Phys. Med. Biol. 63 (2018) 08NT03 (8pp) https://doi.org/10.1088/1361-6560/aab8d2

Physics in Medicine & Biology

IPEM Institute of Physics and Engineering in Medicine

OPEN ACCESS

RECEIVED
3 January 2018

REVISED
15 March 2018

ACCEPTED FOR PUBLICATION
22 March 2018

PUBLISHED
20 April 2018

NOTE

High resolution propagation-based imaging system for *in vivo* dynamic computed tomography of lungs in small animals

M Preissner[1], R P Murrie[1], I Pinar[1], F Werdiger[1], R P Carnibella[2], G R Zosky[3], A Fouras[2,4] and S Dubsky[1]

[1] Department of Mechanical and Aerospace Engineering, Monash University, Melbourne, Victoria, Australia
[2] 4Dx Limited, Melbourne, Victoria, Australia
[3] School of Medicine, Faculty of Health, University of Tasmania, Hobart, Tasmania, Australia
[4] Biomedical Imaging Research Institute, Cedars-Sinai Medical Center, Los Angeles, CA, United States of America

E-mail: melissa.preissner@monash.edu **and** stephen.dubsky@monash.edu

Keywords: 4DCT, in vivo, x-ray imaging, functional imaging, biological imaging, tomography

Supplementary material for this article is available online

Abstract

We have developed an x-ray imaging system for *in vivo* four-dimensional computed tomography (4DCT) of small animals for pre-clinical lung investigations. Our customized laboratory facility is capable of high resolution *in vivo* imaging at high frame rates. Characterization using phantoms demonstrate a spatial resolution of slightly below 50 μm at imaging rates of 30 Hz, and the ability to quantify material density differences of at least 3%. We benchmark our system against existing small animal pre-clinical CT scanners using a quality factor that combines spatial resolution, image noise, dose and scan time. *In vivo* 4DCT images obtained on our system demonstrate resolution of important features such as blood vessels and small airways, of which the smallest discernible were measured as 55–60 μm in cross section. Quantitative analysis of the images demonstrate regional differences in ventilation between injured and healthy lungs.

1. Introduction

Computed tomography is the most widely used clinical imaging technique for investigating lung diseases, owing to its ability to noninvasively resolve the structures within the lung in detail. Four dimensional computed tomography (4DCT) allows the lung structures to be imaged over the breathing cycle, and provides the opportunity for further analysis to calculate functional parameters such as specific ventilation (Brennan *et al* 2015). However, producing high-resolution *in vivo* computed tomography scans of lungs in the pre-clinical laboratory setting remains difficult. Until now, scanners and techniques have suffered from either relatively poor spatial resolution, or require scan times that are prohibitive for practical *in vivo* imaging.

Synchrotron facilities provide excellent imaging of the lungs in small animals, due to their high brilliance and coherence, providing air-tissue contrast through phase-contrast imaging (Kitchen *et al* 2004, Fouras *et al* 2009, 2012, Sera *et al* 2013). Due to the limited accessibility of synchrotron sources, laboratory pre-clinical imaging facilities that are capable of providing high quality imaging would open up new possibilities for studies that require pre-treatment, or for longitudinal studies that require repeated imaging over days or weeks (Krenkel *et al* 2016. Previous studies on *in vivo* CT imaging on a pre-clinical facility show excellent results for phase-contrast (dark-field) imaging in a laboratory setting, albeit with longer exposure times (i.e. 10 s) (Tapfer *et al* 2012, Bech *et al* 2013).

Here we present the development and characterization of a laboratory x-ray system for dynamic *in vivo* imaging of lungs in small animals. Using a high-brightness liquid-metal-jet x-ray source, we have achieved propagation-based phase enhancement to produce high-resolution, four-dimensional computed tomography of mechanically ventilated mice, previously only achievable using synchrotron facilities (Stahr *et al* 2016, Dubsky *et al* 2017). Phase enhancement in the lung tissue acts to improve contrast at the air/tissue interfaces, rather than generating phase fringes (for retrieval). Using phantoms, we characterize the spatial resolution of our system, and demonstrate the contrast resolution for quantitative imaging of the lung.

Accepted quality standards and customized phantoms enable quality control and robust performance testing for clinical cone-beam computed tomography (DIN 2013, Steiding *et al* 2014). Currently, no such standards for pre-clinical (micro-CT) scanners exist. In order to address the issue of quality assurance in micro-CT, Kalender *et al* propose a method that tests a combination of dose, resolution, noise and scan time (Kalender *et al* 2005). To benchmark our system against current scanners, we adopt the quality factor, which amalgamates these important parameters into a single index for comparison between systems. Finally, we present *in vivo* 4DCT images of mouse lungs to demonstrate the quality of imaging that our system achieves for pre-clinical investigations.

2. Methods

2.1. X-ray imaging set-up

Figure 1 shows the laboratory set-up. The high-brightness x-ray source (Excillum D2 + , Excillum AB, Kista, Sweden) has a liquid-metal-jet anode (gallium alloy) which enables higher electron beam power (70 kVp, 250 W) with a micro-focus spot of between 15 and 20 μm. It has a polychromatic x-ray beam with characteristic x-ray peaks at 8 keV and 24 keV (Larsson *et al* 2011). A high-speed flat panel detector (PaxScan 2020, Varian Medical Systems, Palo Alto, CA, USA) is mounted at a distance of 3363 mm from the x-ray source. The geometric magnification (M) is adjusted by translating the stage for the distances R_1 and R_2 (Zaber Technologies, Vancouver, Canada). The detector has a pixel size of 194 × 194 μm and is capable of achieving a frame rate of up to 30 Hz with an 18 ms exposure time.

The range of geometric magnification achievable with the current set-up of this system is 7.2–12.0, where $M = (R_1 + R_2)/(R_1)$. The corresponding range of field of view is between 16.1 and 27 mm. The effective pixel size of the projection images for this magnification range is between 16 and 27 μm. Phase enhancement is achieved via a propagation distance and can be seen in the fringes of the projection image in figure 1(B). The phase enhancement can also be quantified with an effective object-image distance, $z_{eff} = R_1R_2/(R_1 + R_2)$ (Wilkins *et al* 1996, Mayo *et al* 2002). Our set-up has z_{eff} values of between 257 mm and 402 mm, which is a practical compromise between exploiting the phase enhancement our system provides without compromising the flux required for dynamic imaging with short exposure times.

Table 1 shows the two main combinations of x-ray spot size, power and projections per CT used for dynamic lung imaging. The standard setting is based on a larger spot size, fewer projections and lower power (with a lower radiation dose), whereas the maximum setting has a smaller spot size and a higher power, resulting in better image quality (as defined by the quality factor described below), with a higher radiation dose as the trade-off.

2.2. Phantom imaging and dose measurement

Resolution testing was carried out with phantoms. The CT resolution was measured using a line pair phantom (Micro-CT bar pattern phantom, QRM GmbH, Möhrendorf, Germany). A customized 3D printed rod (FullCure720, Objet Eden260V, Stratasys Ltd) was used to test noise. The contrast resolution was tested with a low contrast phantom with three inserts (Micro-CT Low Contrast Phantom V2, QRM GmbH, Germany). The radiation dose rate was measured using a pencil beam dosimeter (TNT 12000WD wireless detector and 500–100 CT ion chamber, Fluke Biomedical, Washington, USA).

2.3. *In vivo* 4DCT imaging

The use of eight-week old BALB/c female mice for *in vivo* imaging was approved by the local Animal Ethics Committee of Monash University (Monash University Research Platform, Melbourne, VIC, Australia) and conducted in accordance with the guidelines set out in the Australian code of practice for the care and use of animals for scientific purposes. Mice were anaesthetized with an intraperitoneal injection of ketamine (Parnell Australia Pty Ltd, Alexandria NSW, Australia) and xylazine (Xylazil-20, Troy Laboratories Pty Ltd, Smithfield NSW, Australia), surgically intubated and placed upright in a custom sample mount with ventilator attachments, which is 3D printed and can therefore be made to the size and shape of the sample, e.g. mouse or small rat. Mice were ventilated at a peak inspiratory pressure of 20 cm H_2O and zero positive end-expiratory pressure with an inspiratory-expiratory ratio of 1:1 (300 ms : 300 ms). The animal was placed on a ventilator (AccuVent, Notting Hill Devices, Melbourne, Australia) and secured on the rotating stage. Image acquisition was synchronized with the ventilator. Projection images were obtained over multiple breath cycles for a 360° rotation of the sample. The respiratory rate of the animal (RR, breaths per minute) determines the number of phases (n) acquired in the 4DCT: $n = 60f/RR$, where f is the image acquisition rate (Hz). The rotational speed of the stage (ω, degrees per second) is determined by the total number of projections required for the 4DCT: $\omega = 360°\ f/np$, where p is the number of projections per phase, i.e. 400 projections for the standard setting or 800 projections for the maximum setting (table 1). The projections are allocated (binned) into discrete phases of the respiratory cycle. The binned projection images are then reconstructed using filtered back-projection based on the Feldkamp–

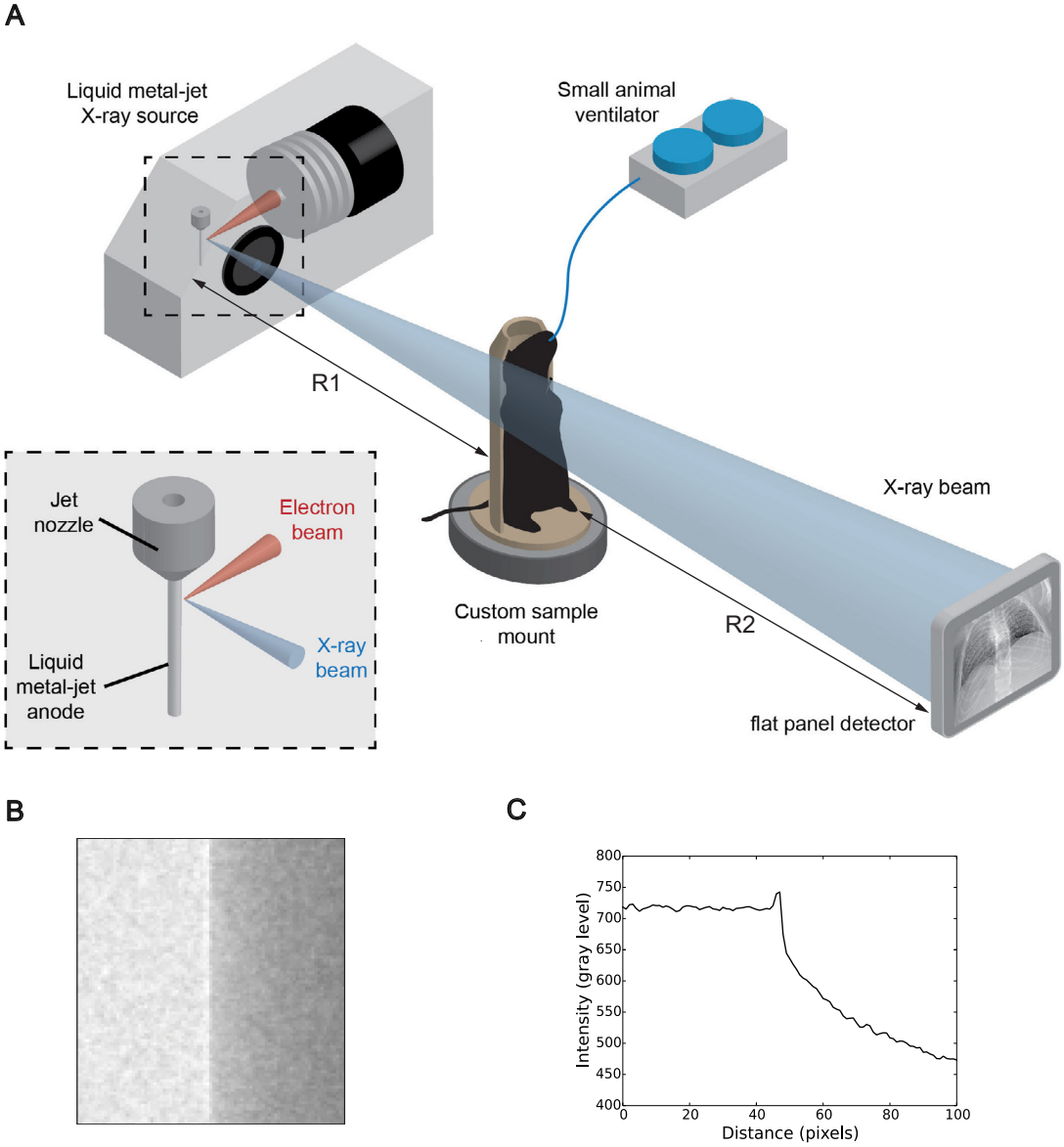

Figure 1. (A) X-ray imaging set-up: polychromatic cone-beam x-rays pass through the sample and the resulting projection images are captured by the high-speed detector at 30 Hz. (B) Close up of projection image of a 20 mm diameter acrylic rod with a geometric magnification of 7.2, acquired at the maximum source setting (see table 1). A phase fringe is visible at the boundary between the air (left) and the rod material (right), and is shown by the vertically averaged profile plot in (C), whereby a spike in intensity at the boundary is observed.

Table 1. X-ray imaging settings used for small animal lung imaging.

Setting	X-ray spot (μm)	Power (W)	Projections per CT	Scan time per CT (s)	Usage
Standard	20	200	400	16	Continuous usage
Maximum	15	250	400–800	16–32	Limited usage

Davis–Kress cone-beam CT reconstruction algorithm to obtain 3D cross-sectional images (Feldkamp *et al* 1984, Yang *et al* 2006).

3. Results and discussion

3.1. CT resolution

The resolution for CT images was tested using a high precision bar pattern (line pair) phantom for micro-CT (QRM GmbH, Möhrendorf, Germany) at the standard and maximum settings (table 1). The images are shown in figure 2. Note that the corner artifacts are due to beam hardening. Based on visual inspection of the line pairs in the image, the spatial resolution lies between 10 line pairs per mm (lp mm^{-1}), i.e. 50 μm line widths, where

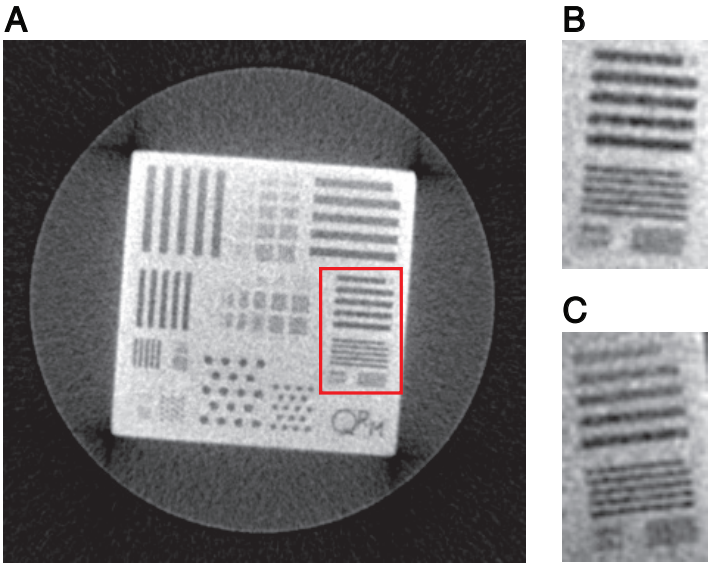

Figure 2. (A) CT slice of QRM micro-CT bar pattern phantom (5 × 5 mm^2 chip) taken at the maximum source setting with 1600 projections and a geometric magnification of 9.2. Contrast adjusted for clarity. Region of interest in red, where line pairs correspond to line widths of 100 μm (5 lp mm^{-1}), 50 μm (10 lp mm^{-1}), 25 μm (20 lp mm^{-1}) and 10 μm (50 lp mm^{-1}). (B) Line pairs in the region of interest at the maximum setting. (C) Lines pairs in the region of interest at the standard setting.

the bars can be resolved, and 20 lp mm^{-1}, i.e. 25 μm line widths, where the bars can no longer be resolved. For a more accurate measure of the spatial resolution, the modulation transfer function (MTF) of the system was calculated based on the standard definition by Boreman (2001). The 10% MTF was calculated as 11 lp mm^{-1} for the standard source setting and 12 lp mm^{-1} for the maximum source setting.

3.2. Radiation dose

Reducing the radiation dose received by the animal is important to avoid unwanted interference in experimental results or ill-effects from radiation, particularly in the case of longitudinal studies (Boone *et al* 2004, Vande Velde *et al* 2015). The dose rate was measured as 5.01 mGy s^{-1} air kerma using a pencil-beam dosimeter (TNT 12000WD wireless detector and 500–100 CT ion chamber, Fluke Biomedical, Washington, USA). The total dose for a CT obtained with the standard setting is 30 mGy, whereas the total dose for a CT on the maximum setting is 60 mGy.

3.3. Low contrast phantom

Figure 3 shows CT images of a phantom with three inserts of low contrast (due to air bubbles) with known contrast levels of −3%, −6% and −9% (+/− 0.1%) as compared to the background material made of a proprietary epoxy resin (QRM GmbH, Möhrendorf, Germany). Each contrast level has three inserts of varying diameter sizes: small (0.5 mm), medium (1 mm) and large (2 mm). Intensity values were measured for each of the inserts (nine in total) using ImageJ software (Schindelin *et al* 2012). The contrast (c) was determined by comparing the intensity values (I) of the inserts to the background material, $c = 1 - ((I_{insert} - I_{air})/(I_{resin} - I_{air}))$. These were plotted against the known contrast values and shows excellent agreement between the measured and known values. This demonstrates that the system is capable of detecting low contrast levels in samples such as the tissue-air contrast found in the lungs.

3.4. Noise

We adopted an approach similar to Kalender *et al* for the calculation of noise for use in their quality factor equation, whereby noise was defined as the standard deviation (in HU) for a 10 mm^2 region of interest in a 32 mm diameter water phantom (Kalender *et al* 2005). We used a 3D printed 24 mm diameter rod (FullCure720, Objet Eden260V, Stratasys Ltd) made of a material that has properties similar to an acrylic, and as such, has properties similar to water (Ionita *et al* 2014). A region of interest was converted to Hounsfield Units (HU) with ImageJ (Schindelin *et al* 2012) using the following relationship between intensity (I) and HU:

$$I = \left(HU + HU_{shift}\right)\left(\frac{65535}{HU_{range}}\right). \quad (1)$$

For our system, the value for HU_{shift} is 3072 and the value for HU_{range} is 8191, based on calibrations of the attenuation coefficient (μ) for water and air at an effective photon energy of 20 keV (Seltzer 1993), and using

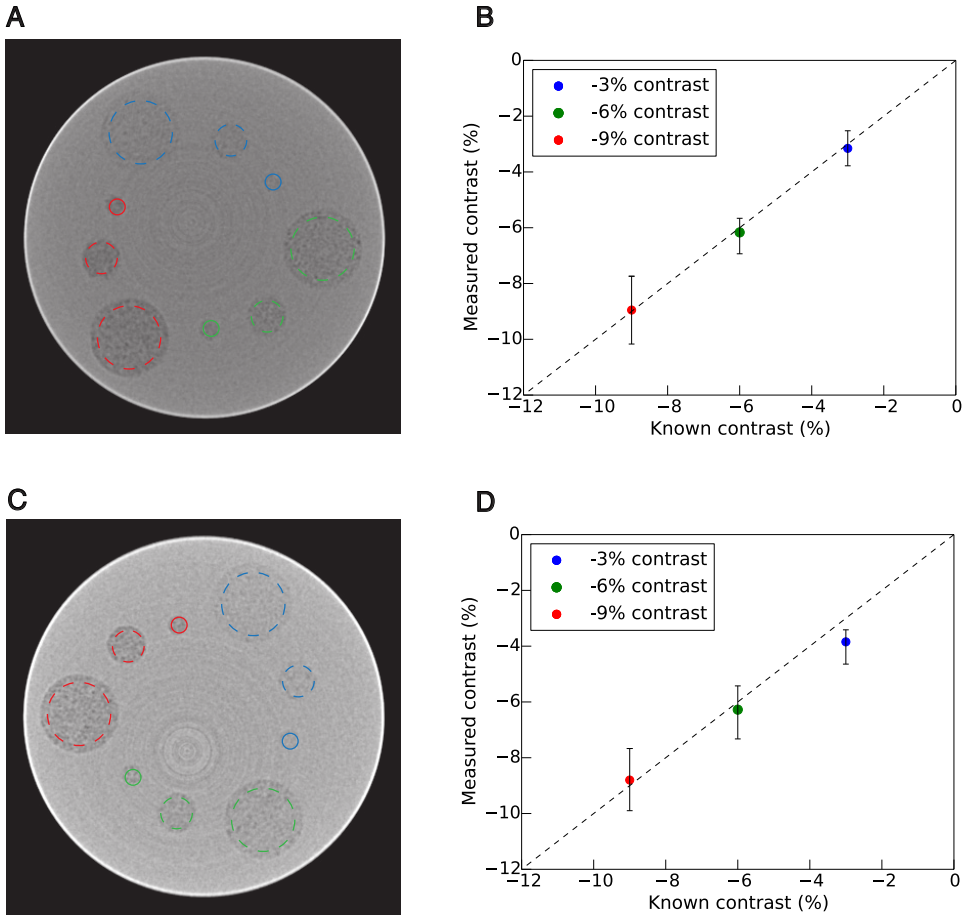

Figure 3. (A) and (C) Low contrast phantom (9 mm diameter) with three inserts (2 mm, 1 mm and 0.5 mm diameter) of known contrast. Dashed circles on the images indicate the location of the inserts. Colors correspond to the contrast levels (red: −9% contrast, green: −6% contrast, blue: −3% contrast). Images taken at 1600 projections per CT, data averaged for 300 slices. Image contrast is adjusted for clarity in the figure. (A) Low contrast phantom image taken at the maximum setting. (B) Data points (mean values) with colors corresponding to the inserts. (C) Low contrast phantom image taken at the standard setting. (D) Data points (mean values) with colors corresponding to the inserts. Error bars in (B) and (D) indicate the minimum and maximum values calculated for each contrast level.

the standard formula for calculating Hounsfield Units: $HU = 1000(\mu_{material} - \mu_{air})/(\mu_{water} - \mu_{air})$ (Kalender 2011). The standard deviation was determined to be 520 HU for the standard setting and 198 HU for the maximum setting, using equation (1).

3.5. Quality factor versus scan time

Kalender *et al* utilize a combination of dose, resolution and noise to characterize various systems in high speed mode and high quality mode, and represent this as the quality factor, Q, given by equation (2): where; $\rho_{10\%} = 10$ % MTF (lp mm^{-1}), $\sigma =$ noise (standard deviation as HU), D = dose (mGy) (Kalender *et al* 2005).

$$Q = 1000\frac{\rho_{10\%}^2}{\sigma\sqrt{D}}. \tag{2}$$

The ratio of quality factor to scan time (Q/T) in high speed mode for one CT is shown in figure 4 for our system for both the standard and maximum settings. These values are compared to four commercially available micro-CT scanners (Scanners (A)–(D) in figure 4) (Kalender *et al* 2005), as well as for a current state-of-the-art commercially available micro-CT scanner (Scanner (E) in figure 4), for which the values of dose (19 mGy), resolution (4.85 lp mm^{-1}) and scan time (26 s, based on 514 projections per CT) were obtained from the current literature and technical notes available from the manufacturer (Behrooz *et al* 2016, Ghani *et al* 2016). The noise for this system was estimated as the same as for the Excillum at the maximum setting (i.e. 198 HU). As scan time increases, the quality factor does not increase. This is due to the squared weighting of the resolution (10% MTF) and the increased dose; longer scan times do not significantly improve resolution, but they do significantly increase the radiation dose received by the sample, thus resulting in a lower quality factor. For terminal *in vivo* imaging, where the dose is less significant than for longitudinal imaging, we compared the devices without the dose component in the quality factor (figure 4(B)), i.e. $Q' = 1000(\rho_{10\%}^2)/\sigma$.

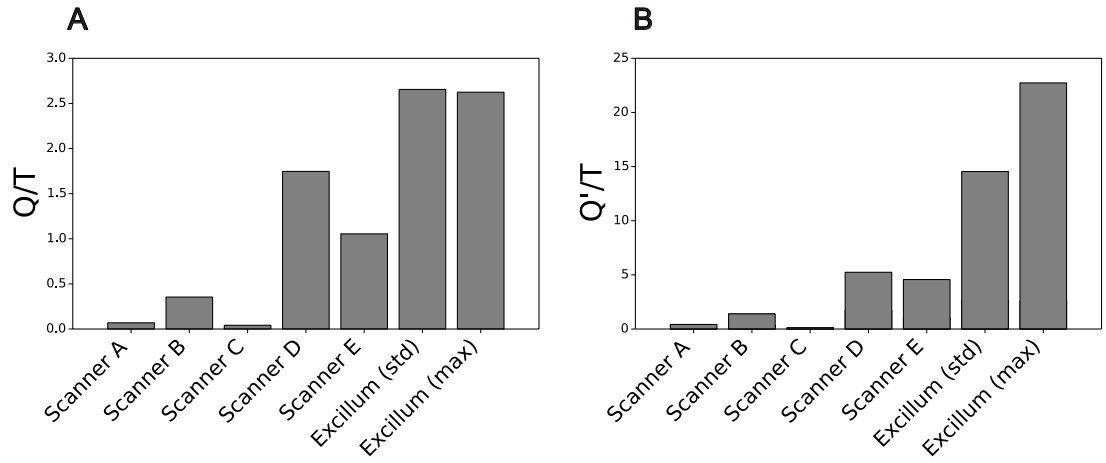

Figure 4. (A) Comparison of scanners in high speed mode using the ratio of quality factor (Q) to scan time (T), Q/T, where the quality factor includes radiation dose. (B) Comparison of scanners in high speed mode without taking dose into account, where Q' does not include dose (e.g. for terminal studies).

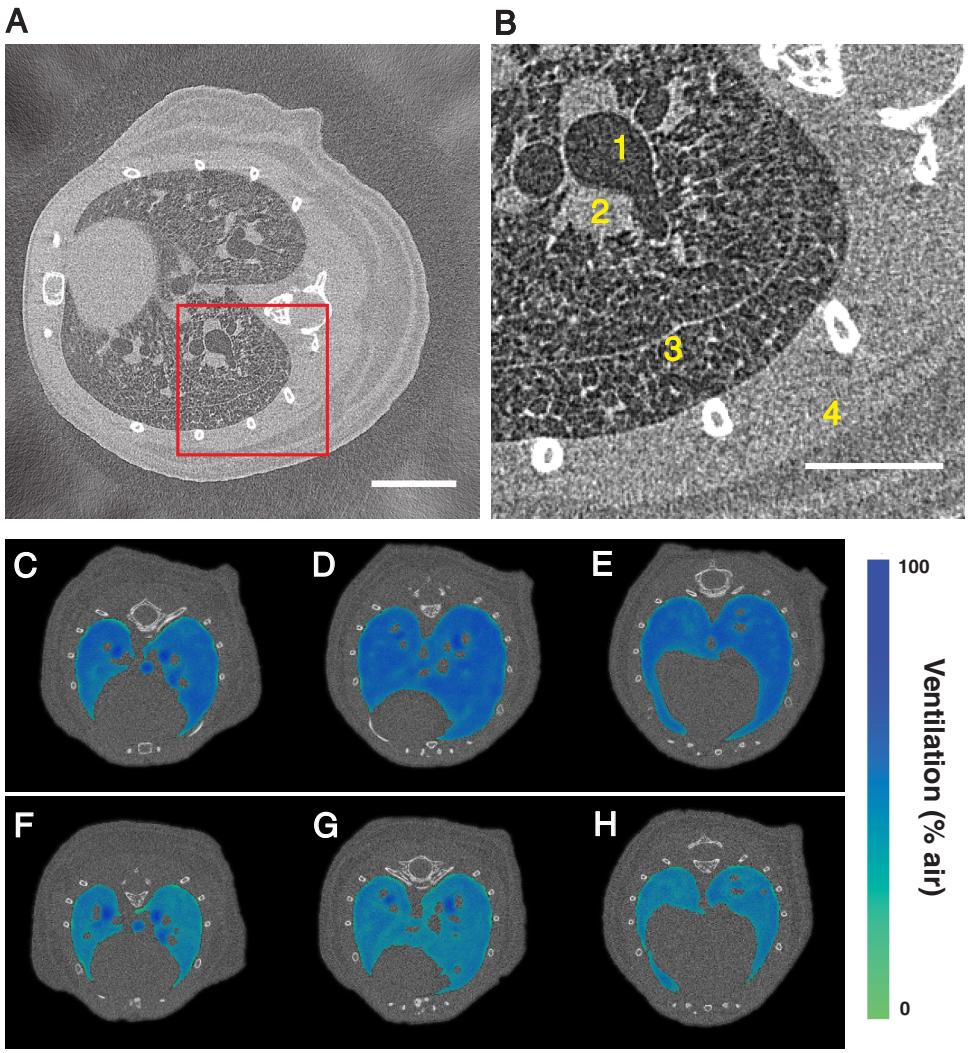

Figure 5. CT slices from 4DCT *in vivo* imaging of BALB/c mice taken at 30 Hz with an 18 ms exposure time (see supplementary material 5). (A) Healthy mouse, with region of interest in red. Scale bar represents 4 mm. (B) Close up of region of interest shows airways (1), blood vessels (2), lobe fissures (3) and fat and muscle layers (4). Scale bar represents 2 mm. (C)–(H) Sequence of CT slices at end-expiration with contours (percentage of air) demonstrating differences in volume of air and distribution of air at 0 hours mechanical ventilation (C)–(E), and after 2 h of high pressure mechanical ventilation (F)–(H).

3.6. *In vivo* 4DCT images of mice

The CT slices in figure 5 are from a typical *in vivo* 4DCT image obtained on our system (supplementary material 5 (stacks.iop.org/PMB/63/08NT03/mmedia)). The images are of healthy BALB/c mice. The images were taken at the maximum setting (table 1), i.e. 800 projections per CT and a scan time of 32 s at an image acquisition rate of 30 Hz and an 18 ms exposure time (with inspiratory and expiratory times of 300 : 300 ms). These *in vivo* CT images demonstrate the high quality images that are achievable with this laboratory set-up. Pertinent features in the lung parenchyma, such as the small airways (or alveolar clusters) can be discerned in our 4DCT images. A selection of these were manually measured (figure 5) using ImageJ and found to be approximately 55–60 μm in cross section, which is consistent with other studies (Irvin and Bates 2003). There are some artifacts (blurring) around the heart and at edges of the lungs and rib-cage bones, due to motion blur (figure 5(A)). The images in figures 5(C)–(H) demonstrate the application of Hounsfield Units for calculating the volume of air in the lungs. In these images, the relative volumes are mapped onto the CT slices. The ability to accurately quantify absolute lung volumes is important in order to determine lung function, for example, in determining the functional residual capacity on a regional level. There are many potential applications for high quality dynamic CT reconstructions, for example to be used for 3D x-ray velocimetry analysis, such as that based on the technique by Dubsky *et al* (2012). High quality images also enable the accurate segmentation of airways (Kim *et al* 2016, Dubsky *et al* 2017) and pulmonary vasculature (Samarage *et al* 2016), which is essential for obtaining regional (e.g. lobar or sub-lobar) information about the lungs in order to determine heterogeneity in disease models (Stahr *et al* 2016).

4. Conclusion

The research presented in this paper demonstrates the optimization of a customized laboratory facility for the purposes of lung x-ray imaging in small animals. The key feature of our system is imaging at high speed with high image quality (10% MTF of 12 lp mm^{-1} for a CT taken at 30 frames per second), which is a prerequisite for functional imaging. The ratio of quality factor to scan time (Q/T) demonstrates that the facility has an excellent balance between imaging speed, resolution, contrast and radiation dose, which is essential for quality control in small animal imaging. Such information is necessary in deciding on the design of future *in vivo* studies with the capabilities of the system in mind and for translation to the clinic. The advantages of a customized in-house facility enables complex and longitudinal animal studies that would otherwise not be possible. Furthermore, the system can be configured and adapted to the specific imaging requirements. For example, the effective propagation distance can be adjusted from pure absorption to phase enhancement, and the magnification and field of view can be configured for specific studies (e.g. mouse, rat), or for a specific region of interest.

Acknowledgments

This work was funded in part by: National Health and Medical Research Council Project Grant 1077905, National Health and Medical Research Council Development Grant APP1055116 and Australian Research Council Discovery Grant DP150102240. C R Samarage for assistance with figure 1. H D Jones for expertise in preparing animals for *in vivo* imaging (figures 5(A) and (B)). E Bennett for preparing animals for *in vivo* imaging (figures 5(C)–(H)). S Irvine for assistance with *in vivo* imaging. K Hourigan for guidance and manuscript editing. This project was also supported by the Multi-modal Australian ScienceS Imaging and Visualization Environment (MASSIVE).

Disclosures

A Fouras, R P Carnibella, S Dubsky and R P Murrie have beneficial interest in 4Dx Limited.

ORCID iDs

M Preissner https://orcid.org/0000-0003-2144-9467
S Dubsky http://orcid.org/0000-0001-8355-7362

References

Bech M, Tapfer A, Velroyen A, Yaroshenko A, Pauwels B, Hostens J, Bruyndonckx P, Sasov A and Pfeiffer F 2013 *In-vivo* dark-field and phase-contrast x-ray imaging *Sci. Rep.* **3** 3209

Behrooz A, Tseng J-C and Meganck J 2016 *Image Resolution in Micro-CT: Principles and Characterization of the Quantum FX and Quantum GX System* (Technical Note)

Boone J M, Velazquez O and Cherry S R 2004 Small-animal x-ray dose from micro-CT *Mol. Imaging* **3** 149–58

Boreman G D 2001 *Modulation Transfer Function in Optical and Electro-Optical Systems* (Bellingham, WA: SPIE Press)

Brennan D *et al* 2015 Clinical validation of 4-dimensional computed tomography ventilation with pulmonary function test data *Int. J. Radiat. Oncol. Biol. Phys.* **92** 423–9
DIN 6868-161 2013 Image quality assurance in diagnostic x-ray departments—part 161: RoV acceptance testing of dental radiographic equipment for digital cone-beam computed tomography
Dubsky S, Hooper S B, Siu K K W and Fouras A 2012 Synchrotron-based dynamic computed tomography of tissue motion for regional lung function measurement *J. R. Soc. Interface* **9** 2213–24
Dubsky S, Zosky G R, Perks K, Samarage C R, Henon Y, Hooper S B and Fouras A 2017 Assessment of airway response distribution and paradoxical airway dilation in mice during methacholine challenge *J. Appl. Physiol.* **122** 503–10
Feldkamp L A, Davis L C and Kress J W 1984 Practical cone-beam algorithm *J. Opt. Soc. Am.* A **1** 612
Fouras A, Kitchen M J, Dubsky S, Lewis R A, Hooper S B and Hourigan K 2009 The past, present, and future of x-ray technology for *in vivo* imaging of function and form *J. Appl. Phys.* **105** 102009
Fouras A, Allison B J, Kitchen M J, Dubsky S, Nguyen J, Hourigan K, Siu K K W, Lewis R A, Wallace M J and Hooper S B 2012 Altered lung motion is a sensitive indicator of regional lung disease *Ann. Biomed. Eng.* **40** 1160–9
Ghani M U, Zhou Z, Ren L, Wong M, Li Y, Zheng B, Yang K and Liu H 2016 Investigation of spatial resolution characteristics of an *in vivo* microcomputed tomography system *Nucl. Instrum. Methods Phys. Res.* **807** 129–36
Ionita C N, Mokin M, Varble N, Bednarek D R, Xiang J, Snyder K V, Siddiqui A H, Levy E I, Meng H and Rudin S 2014 Challenges and limitations of patient-specific vascular phantom fabrication using 3D Polyjet printing *Proc. SPIE Int. Soc. Opt. Eng.* **9038** 90380M
Irvin C G and Bates J H T 2003 Measuring lung function in mice: the challenge of size *Respir. Res.* **4** 1
Kalender W A, Durkee B, Langner O, Stepina E and Karolczak M 2005 Comparative evaluation: acceptance testing and constancy testing for micro-CT scanners *Biomed. Technol.* **50** 1192–3
Kalender W A 2011 *Computed Tomography: Fundamentals, System Technology, Image Quality, Applications* (New York: Wiley)
Kim E H, Preissner M, Carnibella R P, Samarage C R, Bennett E, Fouras A, Zosky G R and Jones H D 2016 Novel analysis of 4DCT imaging quantifies progressive increases in anatomic dead space during mechanical ventilation in mice *J. Appl. Physiol.* **123** 578–84
Kitchen M J, Paganin D, Lewis R A, Yagi N, Uesugi K and Mudie S T 2004 On the origin of speckle in x-ray phase contrast images of lung tissue *Phys. Med. Biol.* **49** 4335–48
Krenkel M, Töpperwien M, Dullin C, Alves F and Salditt T 2016 Propagation-based phase-contrast tomography for high-resolution lung imaging with laboratory sources *AIP Adv.* **6** 035007
Larsson D H, Takman P A C, Lundström U, Burvall A and Hertz H M 2011 A 24 keV liquid-metal-jet x-ray source for biomedical applications *Rev. Sci. Instrum.* **82** 123701
Larsson D H, Lundström U, Westermark U K, Arsenian Henriksson M, Burvall A and Hertz H M 2013 First application of liquid-metal-jet sources for small-animal imaging: high-resolution CT and phase-contrast tumor demarcation *Med. Phys.* **40** 021909
Mayo S C, Miller P R, Wilkins S W, Davis T J, Gao D, Gureyev T E, Paganin D, Parry D J, Pogany A and Stevenson A W 2002 Quantitative x-ray projection microscopy: phase-contrast and multi-spectral imaging *J. Microsc.* **207** 79–96
Samarage C R, Carnibella R, Preissner M, Jones H D, Pearson J T, Fouras A and Dubsky S 2016 Technical note: contrast free angiography of the pulmonary vasculature in live mice using a laboratory x-ray source *Med. Phys.* **43** 6017–23
Schindelin J *et al* 2012 Fiji: an open-source platform for biological-image analysis *Nat. Methods* **9** 676–82
Seltzer S M 1993 Calculation of photon mass energy-transfer and mass energy-absorption coefficients *Radiat. Res.* **136** 147–70
Sera T, Yokota H, Tanaka G, Uesugi K, Yagi N and Schroter R C 2013 Murine pulmonary acinar mechanics during quasi-static inflation using synchrotron refraction-enhanced computed tomography *J. Appl. Physiol.* **115** 219–28
Stahr C S *et al* 2016 Quantification of heterogeneity in lung disease with image-based pulmonary function testing *Sci. Rep.* **6** 29438
Steiding C, Kolditz D and Kalender W A 2014 A quality assurance framework for the fully automated and objective evaluation of image quality in cone-beam computed tomography *Med. Phys.* **41** 31901
Tapfer A *et al* 2012 Experimental results from a preclinical x-ray phase-contrast CT scanner *Proc. Natl Acad. Sci.* **109** 39
Vande Velde G, De Langhe E, Poelmans J, Bruyndonckx P, d'Agostino E, Verbeken E, Bogaerts R, Lories R and Himmelreich U 2015 Longitudinal *in vivo* microcomputed tomography of mouse lungs: no evidence for radiotoxicity *Am. J. Physiol. Lung Cell. Mol. Physiol.* **309** L271–9
Wilkins S W, Gureyev T E, Gao D, Pogany A and Stevenson A W 1996 Phase-contrast imaging using polychromatic hard x-rays *Nature* **384** 335–8
Yang K, Kwan A L C, Miller D F and Boone J M 2006 A geometric calibration method for cone beam CT systems *Med. Phys.* **33** 1695–706